AFRL-RX-WP-JA-2015-0212

ON THE EIGENSTRAIN APPLICATION OF SHOT-PEENED RESIDUAL STRESSES WITHIN A CRYSTAL PLASTICITY FRAMEWORK: APPLICATION TO NI-BASE SUPERALLOY SPECIMENS (POSTPRINT)

William D. Musinski
Materials and Manufacturing Directorate, Air Force Research Laboratory

David L. McDowell
Woodruff School of Mechanical Engineering,

JULY 2015
Interim Report

AIR FORCE RESEARCH LABORATORY
MATERIALS AND MANUFACTURING DIRECTORATE
WRIGHT-PATTERSON AIR FORCE BASE OH 45433-7750
AIR FORCE MATERIEL COMMAND
UNITED STATES AIR FORCE

NOTICE AND SIGNATURE PAGE

Using Government drawings, specifications, or other data included in this document for any purpose other than Government procurement does not in any way obligate the U.S. Government. The fact that the Government formulated or supplied the drawings, specifications, or other data does not license the holder or any other person or corporation; or convey any rights or permission to manufacture, use, or sell any patented invention that may relate to them.

Qualified requestors may obtain copies of this report from the Defense Technical Information Center (DTIC) (http://www.dtic.mil).

AFRL-RX-WP-JA-2015-0212 HAS BEEN REVIEWED AND IS APPROVED FOR PUBLICATION IN ACCORDANCE WITH ASSIGNED DISTRIBUTION STATEMENT.

//Signature//

WILLIAM D. MUSINSKI, Project Engineer
Metals Branch
Structural Materials Division

//Signature//

DANIEL J. EVANS, Chief
Metals Branch
Structural Materials Division

//Signature//

ROBERT T. MARSHALL, Deputy Chief
Structural Materials Division
Materials And Manufacturing Directorate

This report is published in the interest of scientific and technical information exchange and its publication does not constitute the Government's approval or disapproval of its ideas or findings.

REPORT DOCUMENTATION PAGE

Form Approved
OMB No. 0704-0188

1. REPORT DATE *(DD-MM-YY)*	2. REPORT TYPE	3. DATES COVERED *(From - To)*
July 2015	Interim	19 March 2014 – 29 June 2015

4. TITLE AND SUBTITLE
ON THE EIGENSTRAIN APPLICATION OF SHOT-PEENED RESIDUAL STRESSES WITHIN A CRYSTAL PLASTICITY FRAMEWORK: APPLICATION TO NI-BASE SUPERALLOY SPECIMENS (POSTPRINT)

5a. CONTRACT NUMBER
In-House

5b. GRANT NUMBER

5c. PROGRAM ELEMENT NUMBER
62102F

6. AUTHOR(S)
See back.

5d. PROJECT NUMBER
4349

5e. TASK NUMBER

5f. WORK UNIT NUMBER
X0W6

7. PERFORMING ORGANIZATION NAME(S) AND ADDRESS(ES)
See back.

8. PERFORMING ORGANIZATION REPORT NUMBER

9. SPONSORING/MONITORING AGENCY NAME(S) AND ADDRESS(ES)
Air Force Research Laboratory
Materials and Manufacturing Directorate
Wright-Patterson Air Force Base, OH 45433-7750
Air Force Materiel Command
United States Air Force

10. SPONSORING/MONITORING AGENCY ACRONYM(S)
AFRL/RXCM

11. SPONSORING/MONITORING AGENCY REPORT NUMBER(S)
AFRL-RX-WP-JA-2015-0212

12. DISTRIBUTION/AVAILABILITY STATEMENT
Distribution Statement A. Approved for public release: distribution unlimited.

13. SUPPLEMENTARY NOTES
Journal article published in *International Journal of Mechanical Sciences 100 (2015) 195-208*. The U.S. Government is joint author of the work and has the right to use, modify, reproduce, release, perform, display or disclose the work. This report contains color. The final publication is available at http://dx.doi.org/10.1016/j.ijmecsci.2015.06.020.

14. ABSTRACT

Shot-peening-induced compressive residual stresses are often introduced in Ni-base superalloy components to help prevent or retard surface fatigue crack initiation and early growth at near surface inclusions. In certain cases these compressive residual stresses can shift the fatigue crack initiation site from surface to sub-surface locations. However, the ability to computationally predict the improvement in fatigue life response and scatter due to induced compressive residual stresses are lightly treated in the literature. To address this issue, a method to incorporate shot-peened residual stresses within a 3D polycrystalline microstructure is introduced in this work. These residual stresses are induced by a distribution of fictitious orquasi-thermal expansion eigenstrain as a function of depth from the specimen surface. Two different material models are used, a J_2 plasticity and a crystal plasticity model. First, theJ_2 plasticity model with combined isotropic and kinematic hardening is used to determine the distribution of quasi-thermal expansion eigenstrain as a function of depth from the surface necessary to induce the target residual stress profile within the microstructure. This distribution of quasi-thermal expansion eigenstrain is then used within a crystal plasticity framework to model the effect of microstructure heterogeneity on the variability in residual stresses among multiple instantiations. This model is verified with experimental X-ray diffraction (XRD) data for scatter in residual stresses for both the initial microstructure and after a single load/unload cycle.

15. SUBJECT TERMS
crystal plasticity, Ni-base superalloys, IN100, residual stresses, eigenstrain

16. SECURITY CLASSIFICATION OF:			17. LIMITATION OF ABSTRACT:	18. NUMBER OF PAGES	19a. NAME OF RESPONSIBLE PERSON (Monitor)
a. REPORT	b. ABSTRACT	c. THIS PAGE			William D. Musinski
Unclassified	Unclassified	Unclassified	SAR	12	19b. TELEPHONE NUMBER *(Include Area Code)* (937) 255-0485

REPORT DOCUMENTATION PAGE Cont'd

6. AUTHOR(S)

William D. Musinski - Materials and Manufacturing Directorate, Air Force Research Laboratory, Wright-Patterson AFB

David L. McDowell - Woodruff School of Mechanical Engineering, Georgia Institute of Technology, Atlanta GA; School of Materials; Science and Engineering, Georgia Institute of Technology, Atlanta GA

7. PERFORMING ORGANIZATION NAME(S) AND ADDRESS(ES)

Materials and Manufacturing Directorate
Air Force Research Laboratory
Wright-Patterson AFB OH 45433

Woodruff School of Mechanical Engineering
Georgia Institute of Technology
Atlanta GA 30332

School of Materials; Science and Engineering
Georgia Institute of Technology
Atlanta GA 30332

International Journal of Mechanical Sciences 100 (2015) 195–208

Contents lists available at ScienceDirect

International Journal of Mechanical Sciences

journal homepage: www.elsevier.com/locate/ijmecsci

On the eigenstrain application of shot-peened residual stresses within a crystal plasticity framework: Application to Ni-base superalloy specimens

William D. Musinski [a,b,*], David L. McDowell [b,c]

[a] Materials and Manufacturing Directorate, Air Force Research Laboratory, Wright-Patterson AFB, OH 45433, USA
[b] Woodruff School of Mechanical Engineering, Georgia Institute of Technology, Atlanta, GA 30332, USA
[c] School of Materials Science and Engineering, Georgia Institute of Technology, Atlanta, GA 30332, USA

ARTICLE INFO

Article history:
Received 20 February 2015
Received in revised form
22 May 2015
Accepted 29 June 2015
Available online 8 July 2015

Keywords:
Crystal plasticity
Ni-base superalloys
IN100
Residual stresses
Eigenstrain

ABSTRACT

Shot peening induced compressive residual stresses are often introduced in Ni base superalloy components to help prevent or retard surface fatigue crack initiation and early growth at near surface inclusions. In certain cases these compressive residual stresses can shift the fatigue crack initiation site from surface to sub surface locations. However, the ability to computationally predict the improvement in fatigue life response and scatter due to induced compressive residual stresses are lightly treated in the literature. To address this issue, a method to incorporate shot peened residual stresses within a 3D polycrystalline microstructure is introduced in this work. These residual stresses are induced by a distribution of fictitious or quasi thermal expansion eigenstrain as a function of depth from the specimen surface. Two different material models are used, a J_2 plasticity and a crystal plasticity model. First, the J_2 plasticity model with combined isotropic and kinematic hardening is used to determine the distribution of quasi thermal expansion eigenstrain as a function of depth from the surface necessary to induce the target residual stress profile within the microstructure. This distribution of quasi thermal expansion eigenstrain is then used within a crystal plasticity framework to model the effect of microstructure heterogeneity on the variability in residual stresses among multiple instantiations. This model is verified with experimental X ray diffraction (XRD) data for scatter in residual stresses for both the initial microstructure and after a single load/unload cycle.

Published by Elsevier Ltd.

1. Introduction

1.1. Motivation for modeling residual stresses

The beneficial effects of compressive surface residual stresses on high cycle fatigue (HCF) response have been well documented in the literature [1 4]. For Ni base superalloys, a shift from surface dominated to subsurface dominated fatigue crack initia tion sites exists for the transition from low cycle fatigue (LCF) to HCF regimes [5 9]. A similar surface to subsurface transition has been reported for titanium alloys [10,11] and high strength steels [12,13]. In the transition fatigue regime (cycles to failure, $N_f \sim 1 \times 10^4$ 5×10^5 cycles), subsurface initiated fatigue cracks tend to require more cycles to failure as compared to surface initiated fatigue cracks [5]. Accordingly, surface compressive residual stres ses are often introduced in Ni base superalloy components to help prolong/retard fatigue crack initiation [14] and early growth at near surface inclusions and potentially shift fatigue crack initiation sites from surface to subsurface locations [1,2] to increase fatigue life. However, compressive residual stresses are usually only useful in the transition fatigue and HCF ($N_f > 5 \times 10^5$ cycles) regimes since residual stress relaxation at higher applied stress/strain values can eliminate the effectiveness of compressive residual stresses on fatigue life [14 17].

Compressive surface residual stresses can be applied via multi ple techniques (shot/gravity peening, low plasticity burnishing, laser shock peening, etc. [18]). Shot peening is the most commonly used technique in industry to induce compressive residual stresses at the surface, and is the focus of this residual stress study. During the shot peening process multiple high velocity shot beads impact the surface forming multiple indentations and inhomogeneous compressive elastic/plastic deformation of the near surface layer. As such, the resulting residual stress profile is dictated by (1) the

* Corresponding author at: Materials and Manufacturing Directorate, Air Force Research Laboratory, Wright-Patterson AFB, OH 45433, USA. Tel.: +1 937 255 0485.
E-mail address: william.musinski.1@us.af.mil (W.D. Musinski).

http://dx.doi.org/10.1016/j.ijmecsci.2015.06.020
0020-7403/Published by Elsevier Ltd.

interaction between multiple indentations, (2) localized con strained compression, (3) strain rate sensitivity and elastic/plastic response of the material, and (4) local microstructure. In modeling, these discrete impingement events can either be modeled expli citly or idealized as a collective elastic/plastic constrained com pressive loading/unloading event as schematically shown in Fig. 1. The idealization of the multiple impingement shot peening pro cess as a single deformation event is adopted in this paper.

While the influence of residual stress on fatigue life has been reported extensively in the literature, the ability to computation ally predict the improvement in fatigue resistance and change of scatter due to induced compressive residual stresses are lacking in the literature. A significant effort in modeling inclusion and residual stress effects in shot peened martensitic gear steels was undertaken by Prasannavenkatesan et al. [19 22]. They considered separate 3D finite element method (FEM) models at discrete depths subjected to the required amount of compressive load/ unload strain to induce the required residual stress profile at each particular depth. The simulated inclusion sizes ($< 10\ \mu m$) were small compared to the overall 3D FEM model dimensions, so the gradient in applied stress and residual stress over the inclusion was considered to be negligible in their analysis. Alternatively, inclusion sizes in powder metallurgy polycrystalline Ni base superalloy IN100 are on the order of 10 100 μm [6,23,24]. For inclusions of these sizes, the gradient in residual stress (RS) field due to shot peening (Ref. RS profile in [25]) can have a significant effect on stress/strain response and should be considered when analyzing inclusion and RS effects in Ni base superalloys. There fore, a simulation approach that accounts for the entire distribu tion of residual stress, and not just at discrete surface depths, is warranted. Hence, we aim to develop a framework to assess (1) the effect of microstructure on the entire residual stress profile due to shot peening and (2) the effect of cyclic loading on residual stress relaxation in polycrystalline Ni base superalloy components.

This section begins with a brief overview of previous methods to impose residual stresses within components. Next, the eigen strain application of residual stresses within a FEM framework is discussed and a J_2 plasticity model is presented for calibrating this model. Finally, the method by which crystal plasticity is incorpo rated is presented with results for variability of initial residual stress and retained residual stress due to a single load/unload sequence.

1.2. Previous methods for simulated application of residual stresses

Techniques to simulate the shot peening process can be divided into two methods: (1) Simulation of the impact response between the shot bead and the shot peened surface by quasi static or explicit dynamic analyses to predict the resulting residual stress and/or Almen intensity as a function of shot peening parameters (shot size, speed, coverage, material properties, incident angles, etc.) [26 42] and (2) Simulation of the overall induced mechanical response due to shot peening through a deformation process [20,43,44]. Some examples of relevant works regarding these two methods are discussed below.

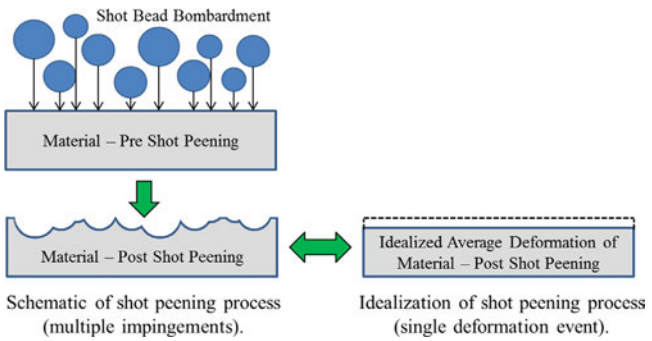

Fig. 1. Schematic showing idealization of shot peening process as a single deformation event.

1.2.1. Simulation of single and multiple impact events

The first means to model the high velocity impact shot peening process focused on single impact events on an elastic plastic target substrate. Chen and Hutchinson [27,28] and Boyce et al. [26] found that explicit dynamic simulations incorporating effects of strain rate sensitivity, inertia, and elastic wave propagation resulted in a better prediction of residual stresses than quasi static analyses. Frija et al. [29] used an energy equivalence expression and 3D quasi static FEM analysis to find good correlation between the predicted residual stress along the shot bead impact centerline and experiments. Zion and Johnson [34] studied the impact of a hard and soft shot bead and a high strength steel and found that the most highly significant input factor was the value of friction coefficient assumed between the shot bead and target material. While these single impact simulations can unveil key relationships between shot peen input (e.g. shot diameter, impact velocity, incident angle) and residual stress output [32], multiple impact events should be used to simulate more realistic peening conditions.

One means to model multiple impacts is to combine discrete element modeling (DEM) and FEM to determine RS profile. DEM simulates spatial interactions/collisions among multiple discrete particles within the shot stream. DEM exports particle/substrate impact velocity, location, and contact forces into a FEM model to calculate resulting plastic strains and residual stresses. Multiple researchers [39 42] have used this combined DEM FEM approach to link the effect of complex part geometry on the overall shot peening process, including the effects of impact angle, impact density, and coverage on location specific residual stress formation.

These combined DEM FEM simulations of multiple impinge ment events are certainly noteworthy. However, it is hard to discern how much variability in local residual stress is attributed to (1) the localized inhomogeneous deformation due to the stochastic impingement events inherent in the shot peening process and (2) the effect of local microstructure, especially grain orientation. Therefore, to isolate the effect of local microstructure, we propose to use a uniform average “amount of impingement” within a crystal plasticity finite element model. In this approach, the individual shot peen events that were modeled in the previous method(s) are not modeled. Instead, the resulting material defor mation and hardening states due to shot peening are (1) induced explicitly within an implicit or explicit FEM model and (2) used as initial conditions for subsequent relaxation/fatigue analysis simulations.

1.2.2. Techniques to induce overall mechanical response due to shot peening

One way to induce residual stresses explicitly within an FEM model is to deform the FEM model in displacement controlled constrained compression. This method mimics the collective mechanical means in which biaxial residual stresses are imposed within a component during the shot peening process and traces the evolution of the material state throughout the deformation process. For example, Prasannavenkatesan et al. [20,21] used a simple displacement controlled method in conjunction with iso tropic plasticity [20] and polycrystal plasticity [21] to induce residual stresses [20] and reproduce experimental trends in

residual stress relaxation [21] due to HCF cyclic bending of a martensitic gear steel. For these analyses, individual 3D FEM models were used at discrete depths and subjected to the required amount of compressive load/unload strain to induce the required residual stress profile at each particular depth. This displacement controlled method presented by Refs. [20,21] is best used for simulated application of residual stresses to the surface of a smooth planar specimen with well defined boundary and loading conditions.

An alternative means to initialize residual stresses within a FEM model is to use the residual stress and material hardening states for target initial conditions. For example, Buchanan et al. [25,45] initialized their material model with an initial material hardening state (effective plastic strain, backstress) and residual stress state based on experimental XRD and cold work measurements at different depths in a Ni base superalloy IN100 material [45]. Similarly, Benedetti et al. [46,47] imposed initial local yield strength and hardening variables at different depths based on the experimental microhardness measurement at that depth. Additionally, the initial residual stress profile was induced by introducing an experimentally fit eigenstrain distribution within the FEM model. The method of introducing eigenstrains within an FEM model to produce residual stresses is covered in more detail next.

1.2.3. Eigenstrain method of imposing residual stresses

Eigenstrains have long been used to model micromechanical misfit strains that are not associated with globally/externally applied mechanical loading. Some examples where eigenstrains are used include internal stresses due to inclusions/particles or fibers [48], differences in coefficient of thermal expansion of different phases/layups [49], phase transformations [50], and heat treatment effects [51]. Several authors have used the eigenstrain method to model/reconstruct residual stresses induced by shot peening [44,52–54], laser shock peening [55–61], and welding [62–66]. For shot peening analysis, the amount of residual stress induced as a function of depth can be controlled by specifying spatial distributions of thermal eigenstrains. The actual residual stress application process is nominally isothermal, so the applied temperature change and thermal expansion eigenstrains are fictitious; they are merely introduced as a means to induce residual stresses within a component under isothermal conditions.

The main challenge of this approach is determining the correct eigenstrain distribution required to produce a given residual stress profile. General solutions/frameworks to the so called "inverse eigenstrain problem" have been developed/presented by many authors [44,52,53,67–69]. Universally, these approaches assume that the eigenstrain distribution can be reconstructed as a superposition of a truncated series of basis functions, i.e.,

$$\varepsilon^*(x) = \sum_{i}^{N} c_i \, \xi_i(x) \tag{1}$$

In this equation, N is the number of basis functions, $\xi_i(x)$, and c_i are the coefficient multipliers for each basis function. The benefit of this model is that one is at liberty to choose the total number of basis functions and the form of each basis function; as a result, there are multiple sets of basis functions that can describe a given eigenstrain distribution. For example, one could use a series of smooth basis functions [67–69], multiple polynomials [44], or even a superposition of multiple kernel density functions including triangular functions [53] or normal distribution functions [52] as the overall eigenstrain distribution estimator. Regardless of the functional form, the most important factor that should be considered is how to solve for the basis function coefficients and whether the given eigenstrain distribution is able to reconstruct the desired residual stress profile. For example, Korsunsky [44] used axisymmetric plate theory to analytically find stresses and deformations arising due to peening and found the necessary eigenstrain as a function of plate depth using polynomial functions as basis functions.

Methods that incorporate both the dynamic material response during residual stress application and the subsequent effect that these residual stresses have on material behavior typically require separate analyses due to different time scales (dynamic shot/laser peen process versus quasi static LCF/HCF/creep loading). For example, Achintha et al. [55–57] combined explicit dynamic and implicit FEM analyses to model the laser shock peening in a Ti 6Al 4 V alloy using an eigenstrain approach and an assumed elastic perfectly plastic material model. They found that although eigenstrain distributions were similar for different specimen thicknesses, the resulting residual stresses were quite different among different specimen thicknesses.

1.3. Objectives, scope and limitations of current work

The previous eigenstrain methods mentioned in the foregoing all suffer from the same shortcomings: they used simple elastic plastic models that are unable to determine the effect of local/random microstructure (e.g. grain size/orientation) on residual stress profile variability and residual stress relaxation. Hence, the objective of this paper is to develop a combined eigenstrain and crystal plasticity finite element simulation approach to address this critical need.

There are many approximations made with regard to the actual shot peening process in our simulations. The process of shot peening involves multiple random shot indentations inducing surface roughness (cf. [15,47,70]). As stated previously, we do not model individual shot peening events. Rather, the collective shot peening process is modeled as a uniform, quasi static displacement event (cf. Fig. 1) that spatially varies as a function of surface depth. The variability in residual stress comes into play due to the microstructure, not due to incomplete coverage or random/sporadic shot locations. In practice, the XRD residual stress measurements are averaged over the irradiated area determined by the size of the X ray beam. The experimental XRD average residual stress data used for comparison in this study was found over an irradiated area of $3\,\text{mm} \times 5\,\text{mm}$ [45], which encompasses over 10,000 grains. Therefore, the highly localized variations in residual stresses due to surface undulations are averaged out for the reported XRD residual stress data. Therefore, we do not simulate the random surface undulations due to the multiple surface impingements induced during the shot peening process. Instead, we impose a uniform "amount of impingement" in each surface layer by means of an applied eigenstrain.

Free surface effects with respect to in plane stress components were neglected/avoided by assuming that the finite element material is from the center of the specimen. The increased hardening of the surface layer of the shot peened material is accounted for in the crystal plasticity finite element model via an increase in dislocation density (and the subsequent increase in yield strength [71]) at the surface.

It should also be noted that the intense amount of near surface cold working and dense dislocation network produced during shot peening can invoke near surface plasticity induced refinement of the microstructure [45,70]. This microstructure refinement is not accounted for in this work. Thus, the purpose of our model is to simulate the overall induced mechanical response due to shot peening, rather than individual impact events or grain refinement.

2. Methodology for imposing residual stresses using eigenstrain approach

The methodology used to impose residual stresses within an eigenstrain framework and its extension to the crystal plasticity finite element method are covered in this section. The quasi thermal expansion distribution can be optimized to fit any targeted/measured residual stress profile. The actual process is isothermal, so the thermal expansion fields are simply used to induce plastic strain gradients and residual stresses. Additionally, this technique has the added benefit that it can be used for more complex material response (e.g., crystal plasticity) and more complex geometries (e.g., notches).

2.1. Material model

2.1.1. Experiments used to calibrate model

During the shot peening process, equibiaxial compressive residual stresses are introduced near the surface due to constrained plastic deformation. To satisfy equilibrium, tensile stresses form within the subsurface of the material. These tensile stresses may decay with increasing depth for thicker specimens [72 74] or approach a steady state value within the bulk of the material for thinner specimens [25,45]. For example, Buchanan et al. [25] performed residual stress relaxation studies of 2 mm thick powder metallurgy (PM) Ni base superalloy IN100 (25 μm average grain size) specimens that were shot peened to an Almen intensity of 6 A. The residual stress profile given in [25] contains average residual stress values measured over a 3 mm × 5 mm irradiated X ray region at given depths from the surface. These measured average residual stress values were fit to a curve of the form [45]

$$\sigma_{RS}(x) = [(\sigma_s \quad \sigma_{int}) + C_1 x]\exp(\quad C_2 x) + \sigma_{int} \tag{2}$$

where the least square values of $\sigma_s = 879.0$, $\sigma_{int} = 205.7$, $C_1 = 67028$, and $C_2 = 20.89$ were determined by Buchanan [45] to fit the experimental residual stress data as a function of depth (x) from the surface. Eq. (2) assumes that the residual stress approaches a steady state internal value of σ_{int} with increasing depth (x) and is applicable for depth values from the surface ($x=0$) to half depth ($x=1$ mm), where the condition of half symmetry is assumed.

Since the work of Buchanan [45] contains information on both the initial residual stress curve and relaxation of residual stresses with fatigue loading and is applied to thinner (2 mm) specimens, we will use Eq. (2) for the initial residual stress curve. Additionally, we limit our computational specimen thickness to 2 mm to ensure that it is consistent with experiments.

2.1.2. Isotropic J_2 plasticity model

A rate independent J_2 plasticity finite element model with combined isotropic/kinematic hardening was used to calibrate the quasi thermal residual stress application approach. The resulting calibrated eigenstrain distribution was later used as an input for a crystal plasticity finite element method (CPFEM) model. The J_2 plasticity model employed is an existing ABAQUS [75] material model that employs the Von Mises yield surface $F = f(\underline{\sigma} \quad \underline{\alpha}) \quad \sigma_{ys} = 0$, where $F = 0$ during plastic flow, $\underline{\sigma}$ and $\underline{\alpha}$ are the stress and back stress tensors, respectively, and σ_{ys} is the Von Mises equivalent yield strength. The function f is given by $f(\underline{\sigma} \quad \underline{\alpha}) = \sqrt{\frac{3}{2}}(\underline{S} \quad \underline{\alpha}) : (\underline{S} \quad \underline{\alpha})$ where $\underline{S}$ is the deviatoric stress tensor. An associated flow rule is assumed as $\dot{\underline{\varepsilon}} = \dot{\bar{\varepsilon}}^p \frac{\partial F}{\partial \underline{\sigma}}$. Here, $\dot{\underline{\varepsilon}}^p$ is the plastic strain rate tensor and $\dot{\bar{\varepsilon}}^p = \sqrt{\frac{2}{3}\dot{\underline{\varepsilon}}^p : \dot{\underline{\varepsilon}}^p}$ is the equivalent plastic strain rate. Cyclic hardening of the yield stress is accounted for by the evolution of isotropic hardening via $\sigma_{ys} = \sigma_o + \kappa_s[1 \quad \exp(\quad b\bar{\varepsilon}^p)]$ [76,77], where σ_o is the yield stress at zero plastic strain, κ_s is the maximum change in the size of the yield surface, and b defines the rate at which cyclic hardening occurs. The evolution of the back stress tensor is characterized by $\dot{\underline{\alpha}}_k = \frac{c_k}{\sigma_{ys}}(\underline{\sigma} \quad \underline{\alpha})\,\dot{\bar{\varepsilon}}^p \quad r_k \underline{\alpha}_k \dot{\bar{\varepsilon}}^p$ [20,75].

For this study, we employ $k=2$ backstress terms ($c_1 = 280{,}900$, $c_2 = 10{,}178$, $r_1 = 1163.8$, $r_2 = 55.65$) to facilitate better stress strain fitting at lower ($k=1$) and higher ($k=2$) strains. This computational model was matched to experimental stress strain data [78] for a coarse grained IN100 Ni base superalloy microstructure. The resulting stress strain plot comparing the computational and experimental data is illustrated in Fig. 2. The optimized isotropic/kinematic hardening parameters for this J_2 plasticity model are listed in the upper left hand corner inset of the Figure. As shown is this Figure, this J_2 plasticity model mimics the cyclic stress strain behavior well for a very complex loading history. Thus, this J_2 plasticity model is deemed sufficient for the calibration of the thermal expansion eigenstrain method to impose residual stresses in smooth specimen components. These results are presented later.

2.1.3. Polycrystal plasticity framework with quasi thermal expansion eigenstrain

This section describes how the concept of quasi thermal expansion eigenstrain finite element method (covered in the next section) was extended in the context of polycrystal plasticity for purposes of imposing a target subsurface residual stress field due to shot peening. The benefit of crystal plasticity relative to the J_2 plasticity model is that it can characterize microstructure variability; a number of different statistically representative microstructure instantiations can be simulated to address the probabilistic fatigue strain life distribution. The goal of this study was to develop a framework to induce a full residual stress profile within a crystal plasticity finite element framework to account for this microstructure variability. Such a framework can be used to assess the effectiveness of shot peening in suppressing near surface crack initiation from inclusions located near to the surface of smooth specimens [79].

To incorporate thermal expansion eigenstrain within the crystal plasticity finite element method under ostensibly isothermal loading conditions, a "quasi" thermal expansion contribution must be included within the deformation gradient. As shown in Fig. 3, the total deformation gradient is assumed to be multiplicatively

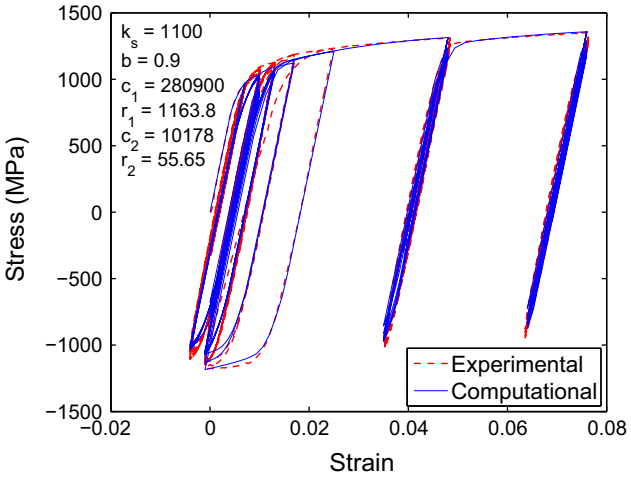

Fig. 2. Comparison of J_2 plasticity model in ABAQUS to experimental data of a coarse grain IN100 cycled at 650 °C. Experimental data are from Ref. [78].

decomposed via

$$\mathbf{F} = \mathbf{F}^e \cdot \mathbf{F}^p \cdot \mathbf{F}^\theta \tag{3}$$

where $\mathbf{F}^e$ denotes elastic distortion and rigid body rotation of the crystal lattice, $\mathbf{F}^p$ accounts for plastic deformation through dis location glide along crystallographic planes, and $\mathbf{F}^\theta$ constitutes thermal expansion. It is noted that temperature change is intro duced *only* to produce an eigenstrain field to induce initial residual stresses from associated elastic plastic deformation. No other properties need be temperature dependent. Isotropic, linearized thermal expansion is assumed, i.e.

$$\mathbf{F}^\theta = \sqrt{1+2\alpha\Delta\theta}\ \mathbf{I} \tag{4}$$

where α is the isotropic thermal expansion coefficient, $\Delta\theta$ is the change in temperature, and $\mathbf{I}$ is the second rank identity tensor. The form of Eqn. (4) was chosen so that the linearized form of the Green finite strain tensor due to thermal expansion, $\mathbf{E}^\theta$, is [80]

$$\mathbf{E}^\theta = \frac{1}{2}\left(\left[\mathbf{F}^\theta\right]^T \cdot \mathbf{F}^\theta \quad \mathbf{I}\right) = \alpha\Delta\theta\ \mathbf{I} \tag{5}$$

The rest of the microstructure sensitive crystal plasticity equations for modeling deformation behavior of a coarse grain IN100 at 650 °C follow those outlined by Przybyla and McDowell [70]. A detailed description of the CPFEM model is omitted in this paper to maintain brevity. We only highlight the incorporation of a quasi thermal expansion deformation gradient ($\mathbf{F}^\theta$) in this section to distinguish what is new/unique in the current CPFEM model relative to the previous IN100 model. More details on the devel opment of the IN100 model and the numerical implementation technique in ABAQUS can be found in the work of Shenoy et al. [78,81] and McGinty [82], respectively.

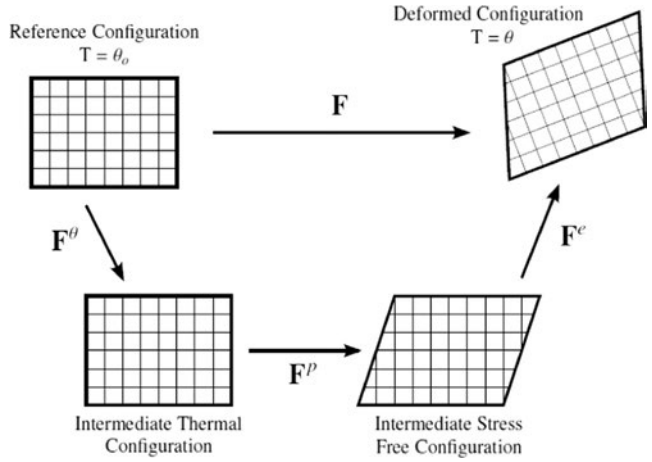

Fig. 3. Multiplicative decomposition of the deformation gradient, including quasi-thermal expansion.

2.2. Finite element model imposition of eigenstrain field

To simulate the material stress state after the shot peening process, a finite element model is used and calibrated to the experimental residual stress XRD data reported by Buchanan et al. [14,25,45,83,84] on a supersolvus PM Ni base superalloy IN100 with an average grain size of 25 μm that was shot peened to a Almen intensity of 6 A. A quasi thermal method of application of residual stresses is chosen in this work because it is easy to apply and calibrate and it is easily extended to more complex models for material response (e.g., crystal plasticity) and more complex geometries (e.g., notches).

2.2.1. Application to J_2 plasticity model

The general methodology for quasi thermal application of residual stresses to a smooth specimen is shown in Figs. 4 and 5 and can be summarized as follows:

1. *Initial configuration*: Fig. 4 shows the finite element model used to simulate residual stress application to a smooth specimen. The experimental smooth specimen [45] had a nominal gage section length, width, and thickness of $y=20$ mm, $z=10$ mm and $x=2$ mm, respectively (see Fig. 4 for x, y, and z directions). Similar to the finite element model employed by Buchanan et al. [25,45], a small portion in the center of this gage section was used for the finite element model. Half symmetry within the depth (x dimension) of the material was employed so that the overall dimensions of the finite element model for J_2 plasticity simulations were $xdim=1$ mm, $ydim=34$ μm, and $zdim=34$ μm. For eigenstrain distribution calibration, the finite element model was divided into many 2.5 μm thick finite elements, as shown in the rightmost image in Fig. 4. It should be noted that since the compressive region of residual stress field is very thin (x depth ~200 μm) and there is a high gradient of residual stress with depth, a very fine finite element thickness of 5 μm is required near the surface to provide convergence of the FEM response. Buchanan [45] reported a similar FEM mesh size requirement for convergence. In this work, a finer mesh of 2.5 μm was used to provide more eigenstrain distribution data points (black dots in Fig. 5) to improve functional form fitting; this fitting is covered later. Each finite element was assigned a given quasi thermal expan sion coefficient α_j and J_2 plasticity material properties. The initial distribution of α_j values was assigned so that the resulting residual stress values were within ±250 MPa from the target residual stress profile at a given depth to avoid any numerical instabilities in the numerical optimization scheme described below.
2. *Eigenstrain application*: with all surfaces constrained from normal displacement, an eigenstrain ($\varepsilon^*_{therm,j} = \alpha_j \Delta T$) is intro duced within the model as shown in the upper left hand corner

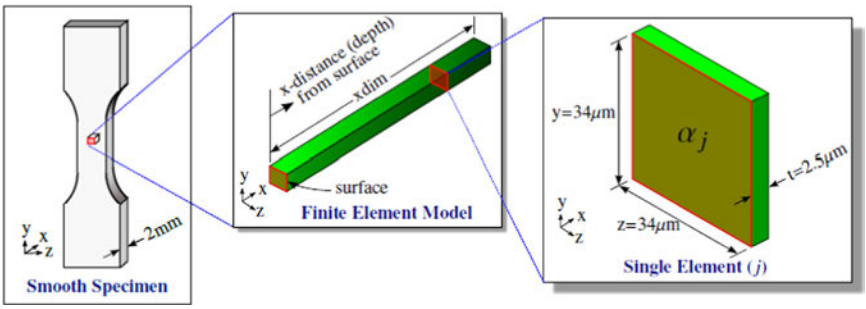

Fig. 4. Finite element model used to apply residual stress to a smooth specimen.

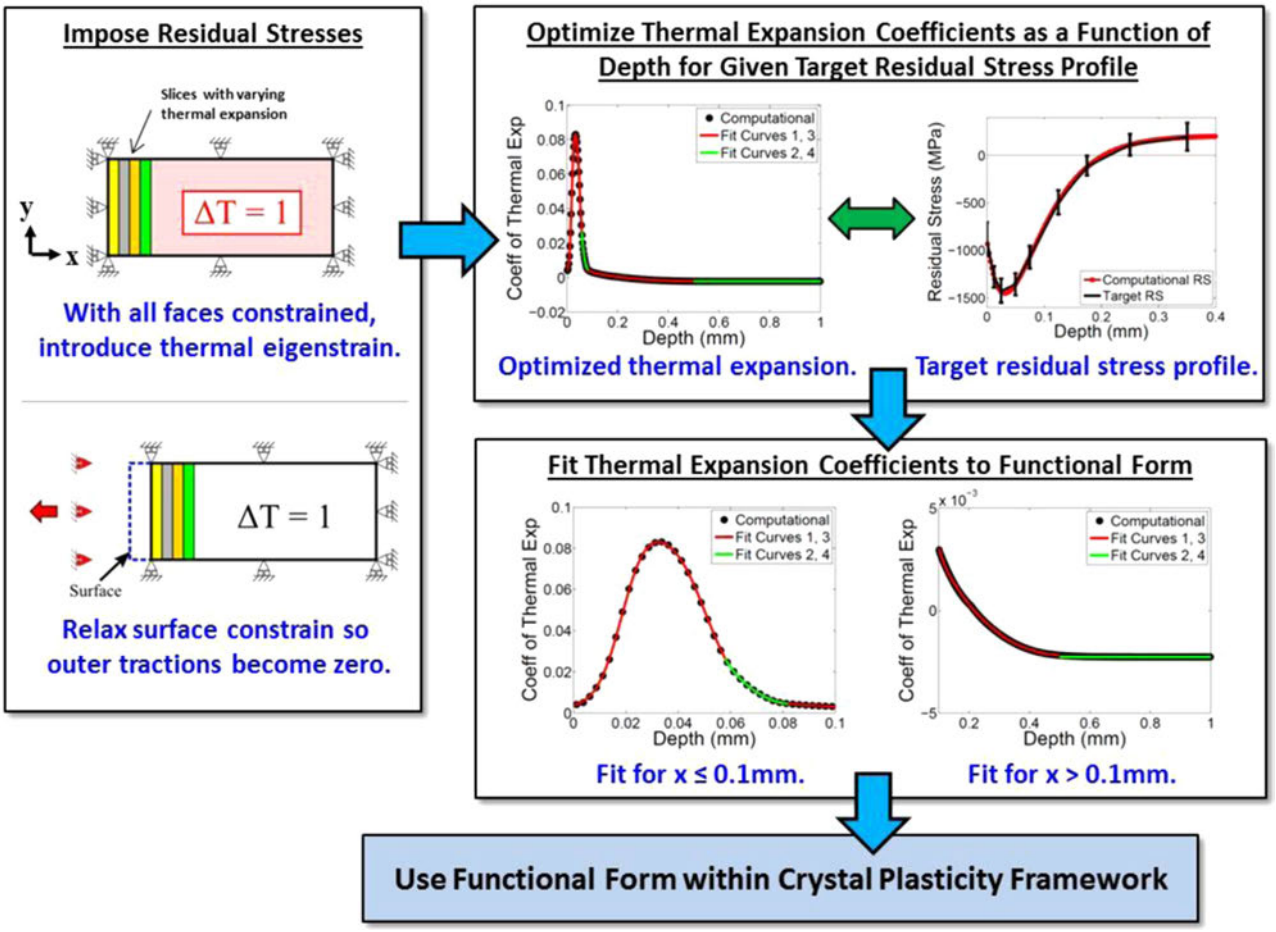

Fig. 5. Methodology for quasi-thermal application of residual stresses to a smooth specimen.

of Fig. 5. It should be noted that an arbitrary value of $\Delta T = 1$ was applied uniformly throughout the whole specimen, with out loss of generality, since temperature is not a physical field variable during the imposition of residual stress.

3. *Release surface constraint*: the surface constraint at $x=0$ is removed to simulate the spring back of the material after shot bead impact (cf. lower left hand portion of Fig. 4). This step is required to relax the stress component normal to the surface so that $\sigma_{xx} \sim 0$, which is representative of the near surface stress state at the end of the shot peening process [20]. This relaxa tion step is analogous to the "unload" step in the displacement controlled method of residual stress application presented by Prasannavenkatesan et al. [20].
4. *Optimization of thermal expansion coefficients*: a secant root finding method [85] is used in conjunction with the FEM model to optimize the spatial distribution of thermal expansion parameters to fit the experimental residual stress profile.
5. *Fit thermal expansion coefficients to functional form*: Gaussian probability density functions and polynomials are used to fit the optimized thermal expansion coefficient as a function of depth from the surface. More details on this functional form and how it is used within the crystal plasticity framework are covered in the following.

2.2.2. Fitting thermal expansion coefficient to functional form

The right hand side of Fig. 5 shows the required thermal expansion as a function of x distance (depth) from the surface that is used to replicate the target residual stress profile shown in the upper right hand portion of Fig. 5. The black dots in Fig. 5 show the optimized thermal expansion coefficient found using the secant root finding method and the red and green solid lines show the functional form fitting of these computationally optimized thermal expansion coefficients. The top middle plot in Fig. 5 displays the entire distribution of thermal expansion coefficient as a function of x distance from the surface. The bottom right two plots in Fig. 5 illustrate zoomed in versions of the fitting of the required thermal expansion coefficient to the piecewise functional forms described below. A piecewise smooth functional form was required so that the thermal expansion coefficients can be defined independent of mesh size and so that this functional form could be used as an input for the crystal plasticity model. The thermal expansion func tion, $\alpha(x)$, was split into 4 sections:

1. $x < 0.058$ mm: this section of the curve was fit using a super position of two Gaussian probability density functions (PDFs). A similar description of using two Gaussian PDFs was demon strated in [52] to describe the eigenstrains induced by shot peening a GW103 magnesium alloy. The functional form used to fit the thermal expansion coefficients at $x < 0.058$ mm is

$$\alpha(x) = A\exp\left[\frac{(x-\mu_B)^2}{2\sigma_C^2}\right] + D\exp\left[\frac{(x-\mu_E)^2}{2\sigma_F^2}\right] + Gx + H \tag{6}$$

2. $0.058 \text{ mm} \le x < 0.082$ mm: this section was fit using a 5th order polynomial:

$$\alpha(x) = a_{21}x^5 + a_{22}x^4 + a_{23}x^3 + a_{24}x^2 + a_{25}x + a_{26} \tag{7}$$

3. 0.082 mm $\leq x <$ 0.5 mm: this section was fit using a 10th order polynomial with coefficients ranging from highest to lowest ranked polynomial terms as $\alpha_{31}, \alpha_{32}, \cdots, \alpha_{39}, \alpha_{310}$.
4. $x \geq$ 0.5 mm: The last section was described by a constant thermal expansion coefficient, α_{41}.

It should be stated that the selection of the x value bounds on these different curves were selected with the constraint that each section pieced together would represent the overall optimized thermal expansion distribution. Each piecewise function mini mized the Euclidean norm (sum of squares error) within its x value bounds. The constants of the two Gaussian PDFs curve were found using a Gauss Newton numerical approach [85] and the constants of the polynomial functions were found using the built in MATLAB "polyfit" function [86]. The constants used for each curve section are listed in Table 1 and the resulting fitting, again, is shown on the right hand side of Fig. 5. These curve demarcations and functional form bounds were chosen for convenience. Any number of functional forms could be used. For example, one could use Eureqa [87,88] to give any number of solutions to this eigenstrain distribution. The main purpose of doing these demar cations is so that we can input these functional forms into the crystal plasticity User MATerial (UMAT) subroutine and induce a given amount of eigenstrain as a function of depth from the surface.

Table 1
Constants used to fit functional form for thermal expansion coefficients as a function of specimen depth.

Curve 1		Curve 2		Curve 3		Curve 4	
Var.	Value	Var.	Value	Var.	Value	Var.	Value
A	0.00051	a_{21}	−4021918	a_{31}	−5450	a_{41}	−0.00227
μ_B	0.0241	a_{22}	147844	a_{32}	14866		
σ_C	0.00764	a_{23}	−26104	a_{33}	−17603		
D	0.00227	a_{24}	15814	a_{34}	11861		
μ_E	0.0377	a_{25}	−580	a_{35}	−5007		
σ_F	0.0130	a_{26}	8.58	a_{36}	1373		
G	0.0557			a_{37}	−24.8		
H	0.0025			a_{38}	27.4		
				a_{39}	−1.79		
				a_{310}	0.0549		

2.2.3. Application to polycrystal plasticity model

Using a similar finite element model as previously described for the J_2 plasticity model, a combined crystal plasticity and J_2 plasticity model was constructed as illustrated in Fig. 6. The polycrystalline grain structure within the crystal plasticity region is constructed using a random sequential adsorption algorithm similar to that described in [71,89,90]. This spherical packing algorithm offers more control over grain sizing as compared to a traditional random seed Voronoi tessellation, which results in a normal distribution. The values of $\mu =$ 0.1 and $\sigma = 0.4$ were chosen for the target lognormal grain size (mean grain size = 34 μm) distribution function, $f(x;\mu,\sigma) = \frac{1}{x\sigma\sqrt{2\pi}}\exp\left[\frac{(\ln x-\mu)^2}{2\sigma^2}\right]$, based on previous publications of fine grain IN100 grain size distributions [71,90 92]. An example of the target grain size distribution and the actual grain size distribution created using the spherical packing algorithm is shown in Fig. 6(a). These grain size distributions are normalized by the mean grain volume, $\langle V_{grn}\rangle = 4/3\pi(0.034\text{ mm})^3 = 1.65\times10^{-3}\text{ mm}^3$.

Fig. 6(b) shows an isometric view of an example polycrystalline grain structure used for the FEM application of residual stresses. In this Figure, each grain is represented by a different color to visualize the grain structure. The FEM model is a square prism of material with a cross section that is 0.17 mm by 0.17 mm, which corresponds to having approximately five grains through the y and z thicknesses of the cross section. Crystal plasticity is employed for elements that are within 0.35 mm of the surface and J_2 plasticity is employed for elements that are at a distance greater than 0.35 mm from the surface to the total x dimension, which is 1 mm in this case.

Fig. 6(c) shows a scaled side view of the example polycrystal line grain structure shown in Fig. 6(b) overlaid on top of the target residual stress profile to compare the assigned FEM material behavior and mesh refinement to the target residual stress profile as a function of depth from the surface. As shown in Fig. 6(c), the refinement in mesh was selected to correspond to key areas in the

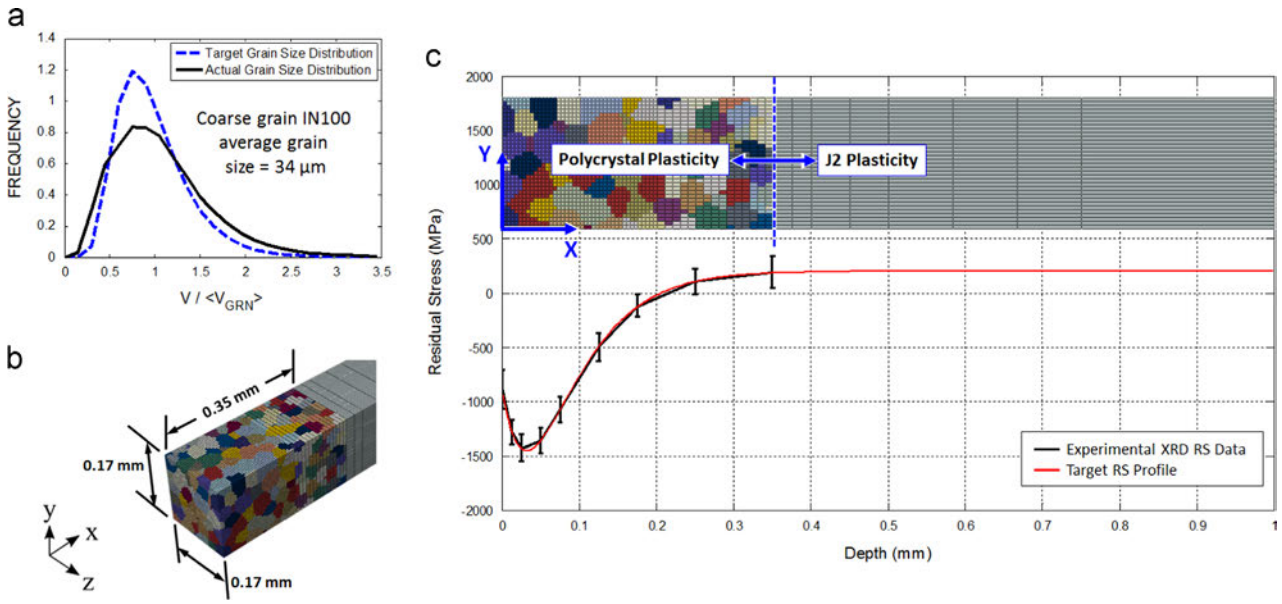

Fig. 6. Example combined polycrystals plasticity and J_2 plasticity finite element model used for eigenstrain-based application of residual stresses. Crystal plasticity is used for depths of $x \leq 0.35$ mm and J_2 plasticity for $x > 0.35$ mm. The experimental XRD residual stress profile is from Buchanan et al. [25] and the target residual stress profile is given by Eq. (2). (a) Target versus actual gain size distribution using random sequential adsorption algorithm, (b) Isometric view of example polycrystalline grain srtucture used for FEM application of residual stress, and (c) scaled side view of example polycrystalline grain structure in (b) overlaid on target RS profile to show assigned material behaviour and and mesh refinement as a function of depth from the surface.

residual stress profile. Since a mesh size of 5 μm provided convergence for the FEM response, this mesh size was used for elements that were within the compressive residual stress zone, $x \leq 0.2$ mm from the surface. Since the experimental residual stress was given up to a depth of $x=0.35$ mm, the crystal plasticity zone was extended up to this depth also. Beyond this depth of $x=0.35$ mm, the residual stress field is relatively flat; thus, J_2 plasticity was used for the zone of $x > 0.35$ mm and the mesh size slowly coarsened out to the depth of $x=1$ mm.

2.3. Method to impose single load/unload sequence

The boundary and loading conditions used during the single, uniaxial load/unload sequence to study residual stress relaxation are shown in Fig. 7. Fig. 7(b) shows 2D projections of the 3D FEM model (Fig. 7(a)) as viewed from the surface (left) and side (right). The loading step starts from the condition where the $x=0$ surface constraint has been released and the stresses in the model have been allowed to relax normal to the surface (ref. bottom left hand side of Fig. 5). Periodic boundary conditions are applied to the lateral surfaces (at $z=0$ and $z=0.17$ mm) using a multi point *Equation constraint in ABAQUS [75]. The bottom surface at $y=0$ and the surface at full FEM depth ($x=1$ mm) are constrained from normal displacement during the load/unload sequence. Rigid body rotation and translation are prevented by constraining z direction displacement for 4 nodes located at coordinates $(x,y,z)=\{(0, 0, 0), (0, 0.17 mm, 0), (1 mm, 0, 0), (1 mm, 0.17 mm, 0)\}$; these 4 node locations are denoted in Fig. 7(b) by the green filled black circles. With these boundary conditions applied, the top surface ($y=0.17$ mm) of the model is subjected to a given net normal traction, $\sigma_{yy,net}=\sigma_a$, and then unloaded to $\sigma_{yy,net}=0$ MPa. During this loading process the top surface is subjected to a multi point constraint (MPC) to make all of the nodes on the top surface displace the same throughout the deformation process.

A MPC displacement controlled method is used for residual stress relaxation studies because residual stress relaxation is most pertinent to strain controlled conditions, e.g., notches. The magnitude of residual stress relaxation will vary depending on the maximum load or displacement applied. Consequently, we study the effect of maximum load/displacement on residual stress relaxation.

3. Results and discussion

3.1. Contour plots of stress in specimens

Fig. 8(b) (e) shows example stress contour plot results for the polycrystalline grain structure depicted in Fig. 8(a). The left hand column of this Figure shows contours of the σ_{yy} component of stress and Von Mises stress at the end of eigenstrain application with all finite element surfaces constrained (upper left of Fig. 5) and the right hand column shows these same contour plots after the surface constraint is released so the outer tractions become zero (lower left of Fig. 5). For comparison purposes, the contour plot scales of the σ_{yy} component plots (Fig. 8(b) and (c)) are identical as well as the contour plot scales for the Von Mises plots (Fig. 8(d) and (e)). These Figures display the ability of the FEM model to induce compressive residual stresses using constrained thermal expansion.

The first thing that is immediately noticed from this contour plot is the high value of σ_{yy} stress (or more precisely, the hydrostatic stress) induced near the surface as the eigenstrain is applied and the faces are constrained (Fig. 8(b)). This high value of hydrostatic stress is typical for a component that is loaded in constrained compression. It is also well known that when a component is loaded in constrained compression, larger strain (or equivalently stress) is required for yielding as opposed to an unconstrained compression condition. In fact, constrained compression can increase the apparent yield strength by a factor of two as compared to unconstrained compression. In these constrained compression cases, a better indicator of plastic response is to use a deviatoric (or equivalent) stress measurement. Hence, both the σ_{yy} and Von Mises stress measures are shown in these plots. Although during the constrained compression step the maximum compressive stress is $\sigma_{yy}=$ 3868 MPa, the Von Mises

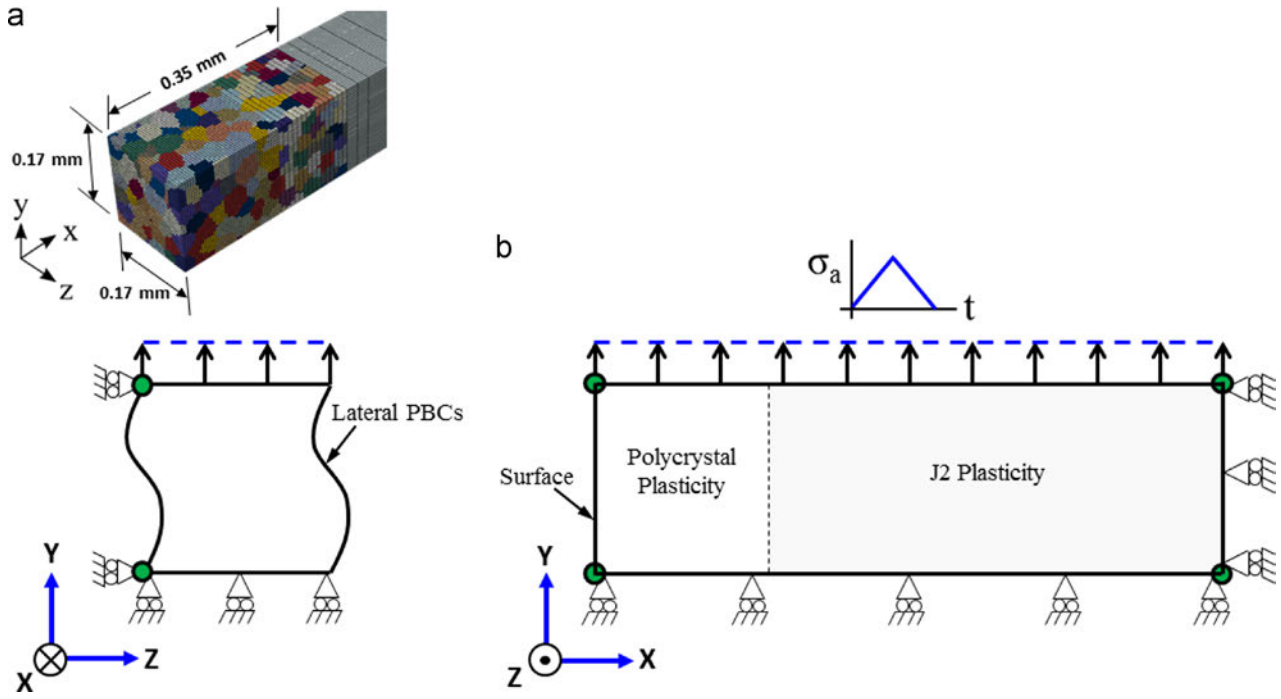

Fig. 7. Schematic of boundary and loading conditions used for single load/unload residual stress relaxation studies. (a) 3D FEM model showing polycrystalline grain structure, and (b) 2D projection of FEM model as viewed from the surface (left) and side (right).

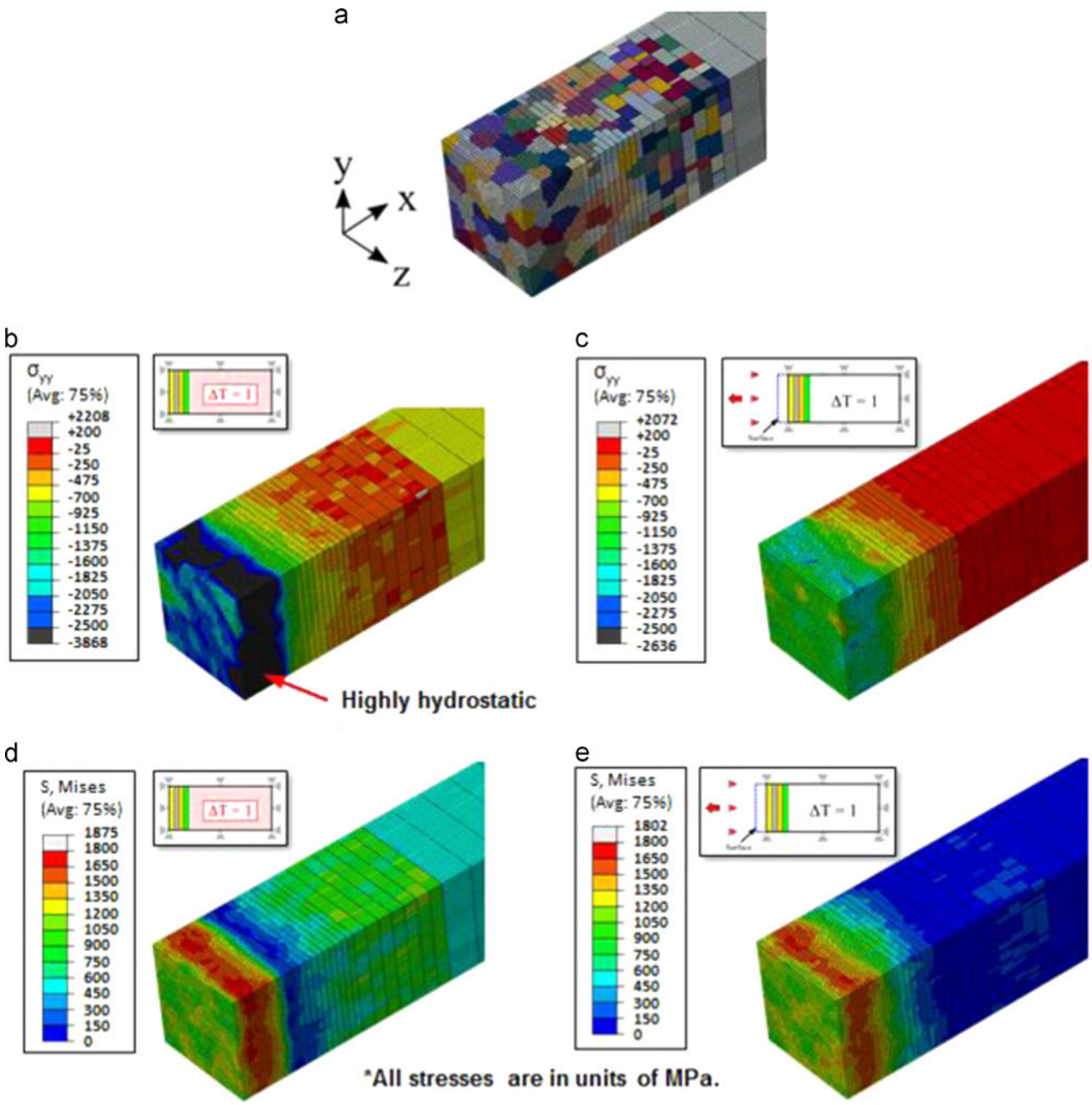

Fig. 8. Example stress contour plot results for conditions before and after surface constraint released. All stresses are in units of MPa. (a) Initial polycrystalline grain structure (0.17 mm x 0.17 mm square cross-section), (b) Contour of σ_{yy} at end of eigenstrain application with all faces constrained, (c) Contour of σ_{yy}after surface constraint has been released, (d) Contour of VM stress at end of eigenstrain application with all faces constrained, and (e) Contour of VM stress after surface constraint has been released.

equivalent stress is at a more reasonable maximum value of 1875 MPa.

The release of the surface constraint on the $x=0$ face (ref. the bottom left portion of Fig. 5) allows the finite element model to expand in the negative x direction. Subsequently, the stress component in the x direction (σ_{xx}) tends toward zero and the σ_{yy} and σ_{zz} components settle into the desired biaxial residual stress values. It should also be noted that after relaxation of the normal surface traction on $x=0$ face, all slices normal to the surface also have net zero σ_{xx} traction into the depth.

3.2. Scatter in residual stress among multiple realizations

In this section, the results from $N=5$ instantiations are presented to determine the amount of scatter exhibited among multiple digitally created microstructures. Due to the different orientation distribution of the grains, the residual stress value of an element at a given depth will differ depending on the orientation of the grain in which the element is located and its interactions between its neighbor grains. Therefore, certain combinations of microstructures will cause the overall residual stress profile to deviate above or below a given ideal/target mean stress value. Plotted in Fig. 9(a) are results from one random microstructure instantiations. In this Figure, each red dot indicates the residual stress value within a single element. Clearly, there is significant scatter in the elemental residual stress values, especially in the near surface area where compressive residual stresses are highest. Since the finite element model employs a structured, voxelated mesh, the residual stress component values at each finite depth (x distance) are averaged and depicted with a blue and green

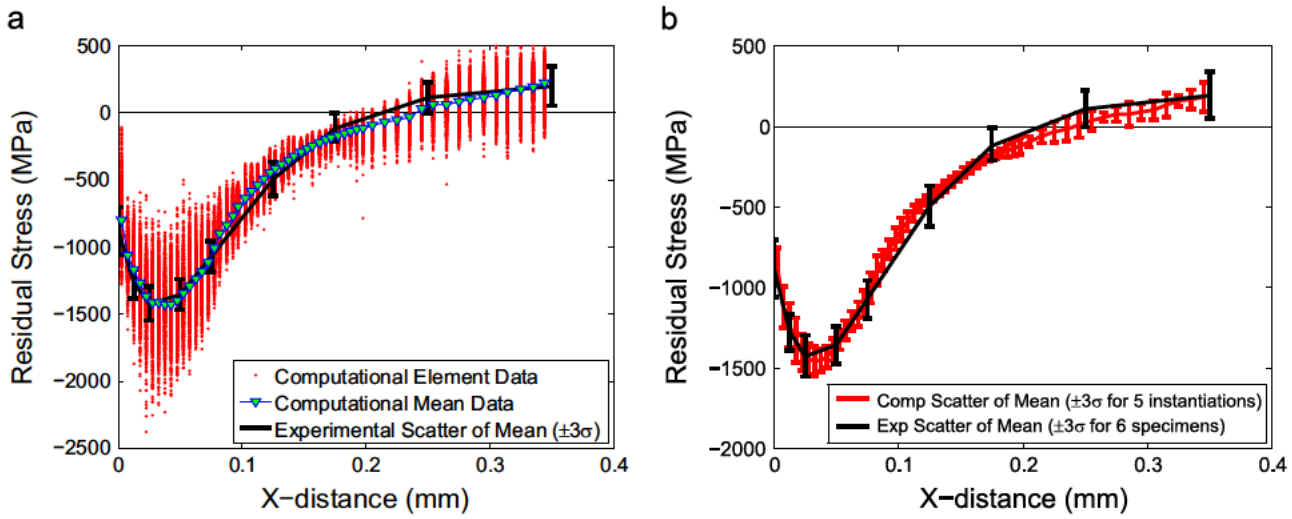

Fig. 9. Computational versus experimental residual stress profile as a function of depth from the surface. Experimental data are from Buchanan et al. [25]. (For interpretation of the references to color in this figure legend, the reader is referred to the web version of this article.) (a) Instantiation 1, and (b) Scatter in RS profile for 5 computational instantiations versus scatter in experimental RS data.

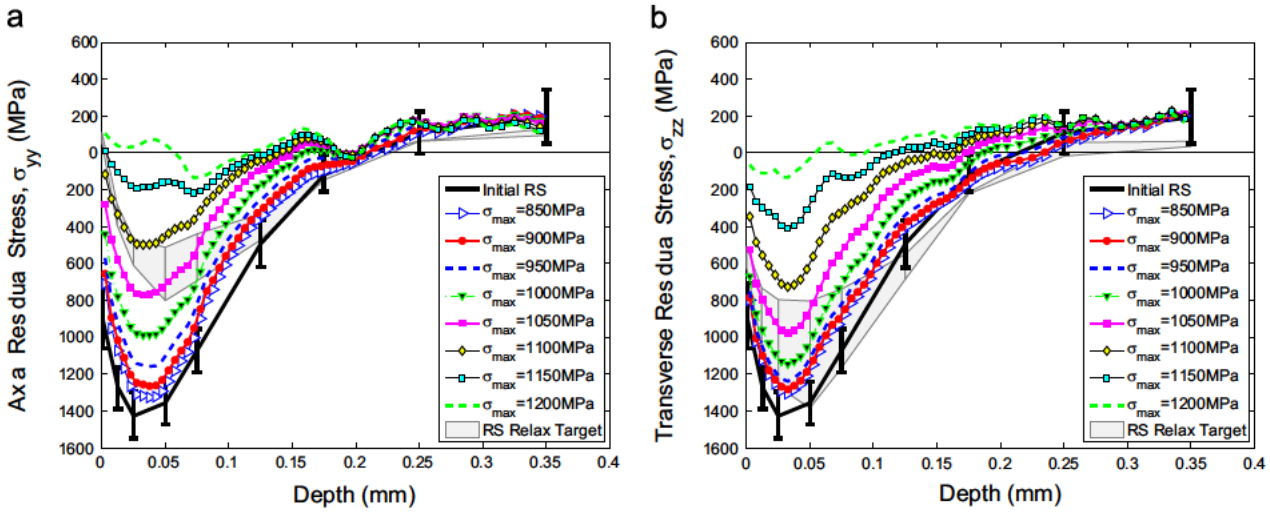

Fig. 10. Simulated residual stress relaxation due to a single load/unload sequence as a function of maximum applied stress. The experimental residual stress target relaxation data measured after one cycle are from Buchanan [45].(a) Axial direction (σ_{yy}). (b) Transverse direction (σ_{zz}).

triangle. Additionally, the target residual stress profile from Buchanan [45] is depicted by the thick black error bar lines. The error bar lines indicate the scatter in average residual stress from six different specimens, where the average residual stress from each specimen is found over an irradiated area of 3 mm × 5 mm [45]. It is clear from this plot that the eigenstrain method of computationally inducing residual stresses within the crystal plasticity framework results in residual stress profiles that are able to match experimental mean values.

Fig. 9(b) compares the experimental data from six baseline XRD measurements [45] to the statistical spread from $N=5$ random instantiations using the polycrystal plasticity model. The typical definition of the standard deviation from a small population are invoked for these $\pm 3\sigma$ values. As shown in Fig. 9(b), there is a strong correlation between the statistical spread of the mean value found from experiments and the statistical spread of the mean value predicted by the crystal plasticity simulations for the near surface ($x < 0.1$ mm) residual stress values. Based on only $N=5$ instantiations, the computational model slightly underpredicts the scatter for locations further into the depth of the smooth specimen. However, the current and future studies focus on the role of residual stresses in suppressing crack formation/propagation near the surface. Therefore, we conclude that the method used here adequately supports these current and future residual stress studies. The utility of this model will further be explored with respect to residual stress relaxation in the following section.

3.3. Residual stress relaxation with single load/unload results

Here we compare the simulated relaxation of residual stresses to experimental residual stress relaxation studies on a coarse grain IN100 at 650 °C with average grain size of 25 μm [45]. Buchanan [45] presented the residual stress relaxation of two specimens in the axial (y loading axis) direction and transverse (z) direction due to a single stress controlled load/unload sequence with $\sigma_{max}=900$ MPa (Ref. [45, Fig. 51]). The spread in XRD measurements of experimental residual stress relaxation in the axial and transverse directions are used for comparison to the simulated residual stress relaxation results presented here.

Pictured in Fig. 10 is the retained σ_{yy} and σ_{zz} residual stress values as a function of depth and maximum applied stress following the simulated load/unload sequence. The top portion

of this Figure shows the relaxation of the axial (σ_{yy}) stress and the bottom portion shows relaxation of the transverse (σ_{zz}) stress due to the single load/unload sequence. As in previous Figures, the initial residual stress is denoted by the thick black error bars. Also, the gray shaded regions in Fig. 10 (a) and (b) correspond, respectively, to the axial and transverse target residual stress relaxation profiles measured by XRD after unloading [45].

The overall trend of the relaxation curves is as expected: there is an increase in residual stress relaxation as the maximum applied stress is increased. When the maximum stress reaches a value of approximately $\sigma_{max}=1150$ MPa, the effect of residual stresses are totally negated in the axial direction. As the peak stress increases to a value of $\sigma_{max}=1200$ MPa, the axial residual stresses become tensile at the surface and go into compression further into the depth ($x>0.4$ mm, which is not depicted in these plots) of the model. Although this depth ($x=0.4$ mm) at which the computational model transitions from tensile to compressive stress is slightly different than the experimental one ($x=0.2$ mm [14], the fact that the computational model predicts this reversal of residual stresses is promising.

Comparing the gray shaded target residual stress relaxation zone (from [45, Fig. 51]) to the computational relaxation curves, there is slight difference in curve shape at depths in the range of $x=0.05$ mm to $x=0.2$ mm. The computational model predicts more relaxation (relatively speaking) in this region as compared to the experimentally measured relaxation in this region. The reason for this difference is currently unknown, but potential reasons for this discrepancy are discussed in the "Limitations" section below.

The predicted residual stress relaxation at the surface of the specimen in the range of $x<0.05$ mm seems to follow the experimental trend, despite the error in the range of $x=0.05$ mm to $x=0.2$ mm. In the surface region, the peak stress required to get in the range of the experimental residual stress relaxation is around $\sigma_{max}=1000$ 1050 MPa for the axial direction and $\sigma_{max}=1100$ MPa in the transverse direction. Since there were a range of values of peak stress that resulted in residual relaxation comparable to experiments, a single peak stress value of $\sigma_{max}=1050$ MPa was used for assessing RS relaxation behavior scatter.

The same $N=5$ instantiations that were used for the residual stress profile scatter in Fig. 9(b) were used to assess scatter of residual stress relaxation. In separate FEM simulations, these finite element models were loaded up to a maximum stress value of $\sigma_{max}=1050$ MPa and then unloaded to zero stress along the y direction. The average residual stress profiles were obtained in the axial and transverse directions. From these values, the statistical spread of the axial and transverse retained residual stresses are plotted in Fig. 11. In this Figure, the left and right columns contain the retained axial and transverse residual stresses, respectively, for maximum applied stress values of 1050 MPa. These simulated values are compared to the statistical spread from 2 separate residual stress relaxation experimental samples from the experimental XRD data reported in Buchanan [45]. Compared to the experimental residual stress profiles [45], the scatter in residual stress of the computational profiles seems to be within a factor of 2 of the experimental profiles. However, this conclusion is quite preliminary as there were only a limited number ($N=2$) of data points from the experiments; it is expected that with more data points, the scatter in residual stress relaxation data would decrease. Further advancement of the residual stress relaxation model would be possible with more experimental and computational replicas.

In the current relaxation study, we only considered relaxation during the first loading cycle. It is well known that relaxation with fatigue cycling occurs in two stages [21]: the majority of residual stress relaxation occurs during the first cycle followed by gradual relaxation with continued fatigue cycling. This two stage relaxation process has been reported for multiple materials in several experimental [93 95] and computational [21,96,97] studies on residual stress relaxation. In the work of Prasannavenkatesan et al. [20,21], they considered the effects of shot peening induced surface residual stresses, pores, and hard and soft primary inclusions in martensitic gear steel on nonlocal fatigue indicator parameters (FIPs) and fatigue crack formation near the inclusions. They concluded that residual stress relaxation could only be modeled using polycrystal plasticity [21].

3.4. Limitations of the CPFEM relaxation model

There are several limitations in this model that can cause errors in the relaxation simulations. First, the computational model contains a domain decomposition of the material into crystal plasticity and J_2 plasticity models. Although these two models were calibrated to the same set of experimental data, the difference in anisotropic crystal plasticity and isotropic J_2 plasticity can cause differences in material stress/strain behavior over the range

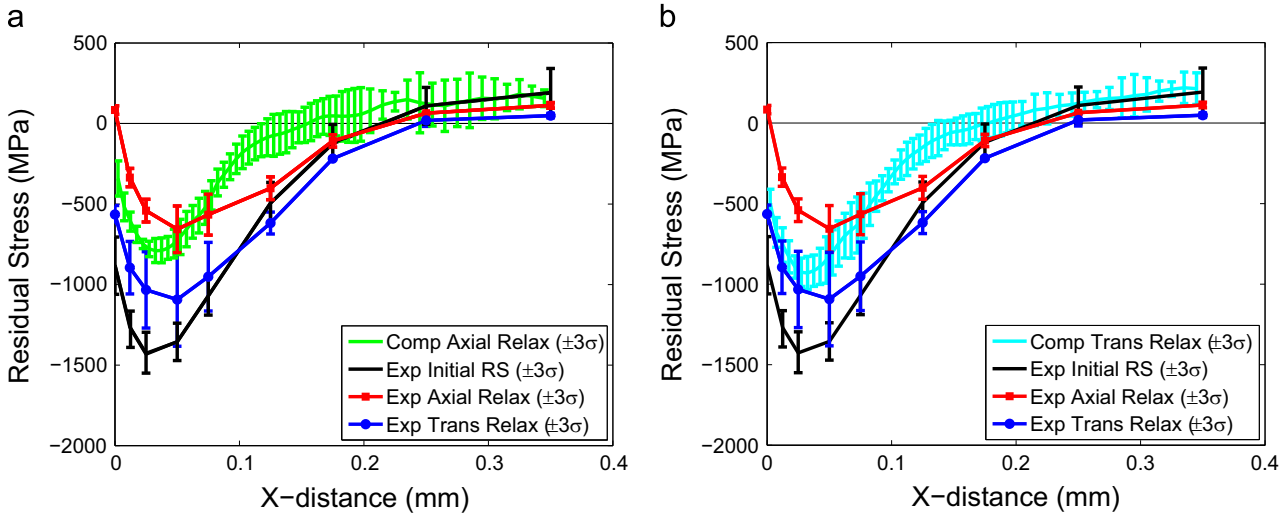

Fig. 11. Simulated versus experimental scatter in residual stress relaxation due to a single load/unload sequence for maximum applied stress σ_{max} 1050 MPa for N 5 instantiations. The experimental residual stress scatter data are from Buchanan [45].(a) Axial (σ_{yy}) relaxation, σ_{max} 1050 MPa, and (b) Transverse (σ_{zz}) relaxation, σ_{max} 1050 MPa.

of several grains. For example, Fig. 9(b) shows that the mean residual stress behavior averaged over a bin size of $x=5$ μm, $y=0.17$ μm, and $z=0.17$ μm can vary up to ~200 250 MPa. This scatter further increases when averaging over individual elements (Fig. 9(a)) or the scale of individual grains. On the other hand, a J_2 plasticity FEM model smears the effect of material anisotropy and predicts a single residual stress profile as a function of depth with no scatter. Additionally, it should be noted that these material models were fit to a coarse grain IN100 with a slightly larger grain size (34 μm) than the IN100 microstructure used for the residual stress experiments (25 μm).

Another potential source of error could be due to the fact that this model is a quasi static representation of a dynamic shot peening process. Shot peening involves high speed collision of many shot beads against a surface. The current model does not take into account such dynamic effects as elastic wave propaga tion, high strain rate effects, or inertia effects; Incorporation of these effects has been shown to provide better residual stress prediction compared to that of a quasi static analysis [26 28]. Additionally, the intense amount of cold working and resulting dense dislocation network produced at the surface can invoke plasticity induced refinement of the microstructure in the surface layer [45,98]. Finer grain structure can affect the yield point/ strength of the material in the thin, highly plastically deformed surface layer; this change in yield point could significantly alter the elastic plastic response of the whole model. This refinement in the microstructure was not accounted for in this work. How ever, the purpose of the current model was to simulate the overall induced mechanical response due to shot peening, rather than individual impact events or grain refinement.

Regardless of these limitations, the current framework is able to reproduce essential aspects of the initial residual stress profile, scatter, and relaxation. While the total profile of the residual stress relaxation curves do not agree precisely with experiments, the simulated relaxation trends near the surface correlate well with experiments. Therefore, the current quasi static eigenstrain appli cation of residual stresses is deemed reasonable for assessing the effect of residual stresses and microstructure on fatigue variability.

4. Summary

In this work, a framework is presented for imposing shot peened residual stresses using computational crystal plasticity. The residual stresses are induced by a distribution of imposed quasi thermal expansion eigenstrains. This distribution was first fit to an experimentally measured residual stress curve using an isotropic J_2 plasticity material behavior and then applied within a crystal plasticity finite element constitutive model. Good correlation between computational and experimental values were obtained for (1) the initial residual stress profile, (2) the scatter in the initial residual stress profile among multiple instantiations, and (3) near surface residual stress relaxation trends for a single load/unload cycle. This method of coupling the effect of microstructure and residual stresses can be used to investigate the effect of certain microstructural features (such as the largest grain, inclusions, pores, etc.) on microstructure sensitive fatigue estimation.

Acknowledgments

WDM is thankful for funding from the Air Force Research Laboratory, United States under contract FA8650 09 2 5800 with the Southwestern Ohio Council for Higher Education. WDM would also like to acknowledge helpful technical discussions with Dennis Buchanan, Reji John, and Andy Rosenberger regarding this work. DLM is grateful for the support of the Carter N. Paden, Jr. Distin guished Chair in Metals Processing.

References

[1] Shiozawa K, Lu L. Very high-cycle fatigue behaviour of shot-peened high-carbon-chromium bearing steel. Fatigue Fract Eng Mater Struct 2002;25(8–9):813–22.
[2] Larsson M, Melander A, Blom R, Preston S. Effects of shot peening on bending fatigue strength of spring steel SS 2090,. Mater Sci Technol Nov. 1991;7:998–1004.
[3] Montross CS, Wei T, Ye L, Clark G, Mai YW. Laser shock processing and its effects on microstructure and properties of metal alloys: a review,. Int J Fatigue 2002;24(10):1021–36.
[4] Peyre P, Fabbro R, Merrien P, Lieurade HP. Laser shock processing of aluminium alloys. Application to high cycle fatigue behaviour. Mater Sci Eng A 1996;210(1–2):102–13.
[5] Deyber S, Alexandre F, Vaissaud J, Pineau A. Probabilistic life of DA718 for aircraft engine disks. In: Eric Ott, Anthony Banik, Joel Andersson, Ian Dempster, Tim Gabb, Jon Groh, Karl Heck, Randy Helmink, Xingbo Liu, Agnieszka Wusatowska-Sarnek, editors. Superalloys 718,625,706 and derivatives. PA, USA: Warrendale; 2005. p. 97–110.
[6] Jha SK, Caton MJ, and Larsen JM. The mean vs life-limiting fatigue response of a Ni-base superalloy, part 1: mechanisms, AFRL-RX-WP-TP-2009–4210; Sep. 2008.
[7] Hyzak JM, Bernstein IM. Effect of defects on the fatigue crack initiation process in two P/M superalloys—1. fatigue origins. Metall Trans Phys Metall Mater Sci 1982;13A(1):33–43.
[8] Hyzak JM, Bernstein IM. Effect of defects on the fatigue crack initiation process in two P/M superalloys—2. surface-subsurface transition. Metall Trans Phys Metall Mater Sci 1982;13A(1):45–52.
[9] Findley K, Saxena A. Low cycle fatigue in rene 88DT at 650 °C: Crack nucleation mechanisms and modeling. Metall Mater Trans A 2006;37(5):1469–75.
[10] Ravi Chandran KS, Jha SK. Duality of the S-N fatigue curve caused by competing failure modes in a titanium alloy and the role of Poisson defect statistics. Acta Mater 2005;53(7):1867–81.
[11] Tokaji K, Ohya K, Kariya H. Subsurface fatigue crack initiation in beta titanium alloys,. Fatigue Fract Eng Mater Struct 2000;23(9):759–66.
[12] Shiozawa K, Hasegawa T, Kashiwagi Y, Lu L. Very high cycle fatigue properties of bearing steel under axial loading condition,. Int J Fatigue May 2009;31 (5):880–8.
[13] Wang QY, Berard JY, Dubarre A, Baudry G, Rathery S, Bathias C. Gigacycle fatigue of ferrous alloys,. Fatigue Fract Eng Mater Struct 1999;22(8):667–72.
[14] John R, Buchanan DJ, Caton MJ, Jha SK. Stability of shot peen residual stresses in IN100 subjected to creep and fatigue loading,. Procedia Eng 2010;2 (1):1887–93.
[15] Barrie RL, Gabb TP, Telesman J, Kantzos PT, Prescenzi A, Biles T, Bonacuse PJ. Effectiveness of shot peening in suppressing fatigue cracking at non-metallic inclusions in Udimet® 720,. Mater Sci Eng A 2008;474(1–2):71–81.
[16] Kirk D., Effects of plastic straining on residual stresses induced by shot-peening, In: Proceedings of the ICSP-3; 1987. p. 213–20.
[17] McClinton M, Cohen JB. Changes in residual stress during the tension fatigue of normalized and peened SAE 1040 steel,. Mater Sci Eng 1982;56(3):259–63.
[18] Prevey PS. The Effect of cold work on the thermal stability of residual compression in surface enhanced IN718, In: Heat Treating: Proceedings of the 20th Conference, vol. 1. St. Louis, MO, United states, 2000. p. 426–434.
[19] Prasannavenkatesan R. Microstructure-sensitive fatigue modeling of heat treated and shot peened martensitic gear steels, PhD Thesis. Georgia Institute of Technology; 2009.
[20] Prasannavenkatesan R, Zhang J, McDowell DL, Olson GB, Jou H-J. 3D modeling of subsurface fatigue crack nucleation potency of primary inclusions in heat treated and shot peened martensitic gear steels,. Int J Fatigue 2009; 31(7):1176–89.
[21] Prasannavenkatesan R, McDowell DL. Polycrystal plasticity modeling of cyclic residual stress relaxation in shot peened martensitic gear steel. J Eng Mater Technol 2010;132(031011):1–8.
[22] Prasannavenkatesan R, Przybyla CP, Salajegheh N, McDowell DL. Simulated extreme value fatigue sensitivity to inclusions and pores in martensitic gear steels,. Eng Fract Mech 2011;78(6):1140–55.
[23] Jha SK, Caton MJ, Larsen JM. The mean vs life-limiting fatigue response of a Ni-base superalloy, part 2: life prediction methodology, AFRL-RX-WP-TP-2009-4212, Sep. 2008.
[24] Jha SK, Caton MJ, Larsen JM. Mean vs. life-limiting fatigue behavior of a nickel-based superalloy. Roger C. Reed, Kenneth A. Green, Pierre Caron, Tim P. Gabb, Michael G. Fahrmann, Eric S. Huron, Shiela A. Woodard (Editors.) Superalloys 2008. Champion, PA, USA; 2008. p. 565–72.
[25] Buchanan DJ, John R, Brockman RA, Rosenberger AH, A coupled creep plasticity model for residual stress relaxation of a shot peened nickel-base superalloy in Superalloys. Roger C. Reed, Kenneth A. Green, Pierre Caron, Tim P. Gabb, Michael G. Fahrmann, Eric S. Huron, Shiela A. Woodard (Editors) 2008. Champion, PA, United States; 2008. 965–74.
[26] Boyce BL, Chen X, Hutchinson JW, Ritchie RO. The residual stress state due to a spherical hard-body impact. Mech Mater 2001;33(8):441–54.
[27] Chen X, Hutchinson JW. Foreign object damage and fatigue crack threshold: cracking outside shallow indents. Int J Fract 2001;107(1):31–51.

[28] Chen X, Hutchinson JW. Particle impact on metal substrates with application to foreign object damage to aircraft engines. J Mech Phys Solids 2002;50 (12):2669–90.
[29] Frija M, Hassine T, Fathallah R, Bouraoui C, Dogui A. Finite element modelling of shot peening process: prediction of the compressive residual stresses, the plastic deformations and the surface integrity. Mater Sci Eng A 2006;426(1–2):173–80.
[30] Schulze V, KlemenzM, and ZimmermannM. State of the art in shot peening simulation. In: Proceedings of the ICSP-10, Tokyo, Japan; 2008.
[31] Zimmermann M, SchulzeV, Baron HU, and LoheD. A novel 3D finite element simulation model for the prediction of the residual stress state after shot peenine. In: Proceedings of the ICSP-10, Tokyo, Japan; 2008.
[32] Hong T, Ooi JY, Shaw BA. A numerical study of the residual stress pattern from single shot impacting on a metallic component. Adv Eng Softw 2008;39:743–56.
[33] Guagliano M. Relating Almen intensity to residual stresses induced by shot peening: a numerical approach. J Mater Process Technol 2001;110:277–86.
[34] Zion HL, Johnson WS. Parametric two-dimensional finite element investigation: shot peening of high-strength steel. AIAA J 2006;44(9):1973–82.
[35] Hong T, Ooi JY, Shaw B. A numerical simulation to relate the shot peening parameters to the induced residual stresses. Eng Fail Anal 2008;15:1097–110.
[36] Mylonas GI, Labeas G. Numerical modelling of shot peening process and corresponding products: residual stress, surface roughness and cold work prediction,. Surf Coat Technol 2011;205:4480–94.
[37] Kim T, Lee JH, Lee H, Cheong S-K. An area-average approach to peening residual stress under multi-impacts using a three-dimensional symmetry-cell finite element model with plastic shots. Mater Des 2010;31:50–9.
[38] Kim T, Lee H, Kim M, Jung S. A 3D FE model for evaluation of peening residual stress under angled multi-shot impacts,. Surf Coat Technol 2012;206:3981–8.
[39] Bhuvaraghan B, Srinivasan SM, Maffeo B, McClain RD, Potdar Y, Prakash O. Shot peening simulation using discrete and finite element methods,. Adv Eng Softw. 2010;41:1266–76.
[40] Badreddine J, Rouhand E, Micoulaut M, Remy S. Simulation of shot dynamics for ultrasonic shot peening: Effects of process parameters,. Int J Mech Sci 2014;82:179–90.
[41] Calle MAG, Alves M. Multibody modeling of the shot peening process. J Braz Soc Mech Sci Eng 2014;36:111–24.
[42] Murugaratnam K, Utili S, Petrinic N. A combined DEM-FEM numerical method for shot peening parameter optimisation. Adv Eng Softw 2015;79:13–26.
[43] Satraki M, Evans A, King A, BrunoG, and WithersPJ. Eigenstrain generated by shot peening in Udimet 720Li inferred by means of finite element and analytical models. In: Proceedings of the ICSP-9; 2005. p. 442–47.
[44] Korsunsky AM. On the modelling of residual stresses due to surface peening using eigenstrain distributions,. J Strain Anal Eng Des 2005;40(8):817–24.
[45] Buchanan DJ. A coupled creep-plasticity model for residual stress relaxation of a shot-peened nickel-base superalloy, (PhD. Thesis). University of Dayton; 2007.
[46] Benedetti M, Fontanari V, Monelli BD. Numerical simulation of residual stress relaxation in shot peened high-strength aluminum alloys under reverse bending fatigue,. J Eng Mater Technol 2010;132011012-1–011012-9.
[47] Benedetti M, Fontanari V, Santus C, Bandini M. Notch fatigue behaviour of shot peened high-strength aluminium alloys: experiments and predictions using a critical distance method. Int J Fatigue 2010;32(10):1600–11.
[48] Baimpas N, Lunt AJG, Dolbnya IP, Dluhos J, Korsunsky AM. Nano-scale mapping of lattice strain and orientation inside carbon core SiC fibres by synchrotron X-ray diffraction. Carbon 2015;79:85–92.
[49] Mura T. Micromechanics of defects in solids. Netherlands: Springer; 1987 (2nd edition).
[50] Jegou S, Barrallier L, Kubler R. Phase transformation and induced volume changes in a nitrided ternary Fe-3%Cr-0.345%C alloy. Acta Mater 2010;58:2666–76.
[51] Depouhon P, Sprauel J-M, Mailhe M, Mermoz E. Mathematical modeling of residual stresses and distortions induced by gas nitriding of 32CrMoV13 steel. Comput Mater Sci 2014;82:178–90.
[52] Song X, Liu WC, Belnoue JP, Dong J, Wu GH, Ding WJ, Kimber SAJ, Buslaps T, Lunt AJG, Korsunsky AM. An eigenstrain-based finite element model and the evolution of shot peening residual stresses during fatigue of GW103 magnesium alloy. Int J Fatigue 2012.
[53] Jun T-S, Korsunsky AM. Evaluation of residual stresses and strains using the Eigenstrain Reconstruction Method. Int J Solids Struct Jun. 2010;47(13):1678–86.
[54] Chaise T, Li J, Nelias D, Kubler R, Taheri S, Douchet G, Robin V. Modelling of multiple impacts for the prediction of distortions and residual stresses induced by ultrasonic shot peening (USP). J Mater Process Technol 2012;212:2080–90.
[55] Achintha M, Nowell D, Fufari D, Sackett EE, Bache MR. Fatigue behaviour of geometric features subjected to laser shock peening: experiments and modelling,". Int J Fatigue 2014;62:171–9.
[56] Achintha M, Nowell D. Eigenstrain modelling of residual stresses generated by arrays of LSP shots. Procedia Eng 2011;10:1327–32.
[57] Achintha M, Nowell D. Eigenstrain modelling of residual stresses generated by laser shock peening. J Mater Process Technol. 2011;211:1091–101.
[58] Dewald AT, Hill MR. Eigenstrain-based model for prediction of laser peening residual stresses in arbitrary three-dimensional bodies. Part 1: model description,". J Strain Anal Eng Des 2009;44(1):1–11.
[59] Korsunsky AM. Residual elastic strain due to laser shock peening: modelling by eigenstrain distribution. J Strain Anal Eng Des 2006;41(3):195–204.
[60] King A, Steuwer A, Woodward C, Withers PJ. Effects of fatigue and fretting on residual stresses introduced by laser shock peening. Mater Sci Eng A 2006;435–436:12–8.
[61] Hu Y, Grandhi RV. Efficient numerical prediction of residual stress and deformation for large-scale laser shock processing using the eigenstrain methodology. Surf Coat Technol 2012;206(15):3374–85.
[62] Lee H, Nakamura H, Kobayashi H. Utilization of thermo-elasto-plastic analysis of welding eigenstrain for improvement of the bead flush method. Eng Fract Mech 2004;71(15):2245–55.
[63] Matos CG, Dodds RH. Modeling the effects of residual stresses on defects in welds of steel frame connections. Eng Struct 2000;22(9):1103–20.
[64] Liljedahl CDM, Zanellato O, Fitzpatrick ME, Lin J, Edwards L. The effect of weld residual stresses and their re-distribution with crack growth during fatigue under constant amplitude loading. Int J Fatigue 2010;32(4):735–43.
[65] Liljedahl CDM, Brouard J, Zanellato O, Lin J, Tan ML, Ganguly S, Irving PE, Fitzpatrick ME, Zhang X, Edwards L. Weld residual stress effects on fatigue crack growth behaviour of aluminium alloy 2024-T351. Int J Fatigue 2009;31 (6):1081–8.
[66] Korsunsky AM, Regino GM, Nowell D. Variational eigenstrain analysis of residual stresses in a welded plate. Int J Solids Struct 2007;44(13):4574–91.
[67] Cao YP, Hu N, Lu J, Fukunaga H, Yao ZH. An inverse approach for constructing the residual stress field induced by welding. J Strain Anal Eng Des 2002;37 (4):345–59.
[68] Qian X, Yao Z, Cao Y, Lu J. An inverse approach for constructing residual stress using BEM. Eng Anal Bound Elem 2004;28:205–11.
[69] Qian X, Yao Z, Cao Y, Lu J. An inverse approach to construct residual stresses existing in axisymmetric structures using BEM. Eng Anal Bound Elem 2005;29:986–99.
[70] Przybyla CP, McDowell DL. Microstructure-sensitive extreme value probabilities for high cycle fatigue of Ni-base superalloy IN100. Int J Plast 2010;26(3):372–94.
[71] Child DJ, West GD, Thomson RC. Assessment of surface hardening effects from shot peening on a Ni-based alloy using electron backscatter diffraction techniques. Acta Mater. 2011;59(12):4825–34.
[72] Webster GA, Ezeilo AN. Residual stress distributions and their influence on fatigue lifetimes. Int J Fatigue 2001;23:S375–83.
[73] Tufft MK.. Shot peen impact on life, part 3: development of a fracture mechanics/threshold behavior predictive model. In: Proceedings of the ICSP-7, Warsaw, Poland; 1999. p. 264–73.
[74] Tufft MK. Modeling of fatigue behavior due to shot peening conditions. In: Proceedings of the ICSP-8, Munich, Germany; 2002. p. 530–39.
[75] ABAQUS. Standard user's manual. Providence, RI: Simulia; 2012.
[76] Chaboche JL. Constitutive equations for cyclic plasticity and cyclic viscoplasticity. Int J Plast 1989;5(3):247–302.
[77] Khan AS, Huang S. Continuum theory of plasticity. New York, NY: John Wiley & Sons, Inc.; 1995.
[78] Shenoy M, Tjiptowidjojo Y, McDowell D. Microstructure-sensitive modeling of polycrystalline IN 100. Int J Plast 2008;24(10):1694–730.
[79] Musinski WD. Modeling the effects of shot-peened residual stresses and inclusions on microstructure-sensitive fatigue of Ni-base superalloy components, (Ph.D. Thesis). Georgia Institute of Technology; 2014.
[80] Malvern LE. Introduction to the mechanics of a continuous medium. Englewood Cliffs, NJ: Prentice-Hall, Inc.; 1969.
[81] Shenoy MM. Constitutive modeling and life prediction in Ni-base superalloys, (Ph.D. Thesis). Georgia Institute of Technology; 2006.
[82] McGinty RD. Multiscale representation of polycrystalline inelasticity, (Ph.D. Thesis). Georgia Institute of Technology; 2001.
[83] Buchanan DJ, John R, Brockman RA. Relaxation of shot-peened residual stresses under creep loading. J Eng Mater Technol 2009;131(3) 031008-1–031008-10.
[84] Buchanan D, John R, Brockman R, Rosenberger A. "A coupled creep plasticity model for residual stress relaxation of a shot-peened nickel-based superalloy,". J Miner Met Mater Soc 2010;62(1):75–9.
[85] Chapra SC, Canale RP. Numerical methods for engineers. New York, NY: McGraw-Hill; 2002.
[86] MATLAB. User's manual. Natick, MA: The MathWorks, Inc.; 2012.
[87] Schmidt M, Lipson H. Distilling Free-Form Natural Laws from Experimental Data. Science 2009;324(5923):81–5.
[88] Schmidt M and LipsonH, Eureqa. www.nutonian.com, 2014.
[89] Groeber M, Ghosh S, Uchic MD, Dimiduk DM. A framework for automated analysis and simulation of 3D polycrystalline microstructures.: Part 1: statistical characterization. Acta Mater 2008;56(6):1257–73.
[90] Groeber M, Ghosh S, Uchic MD, Dimiduk DM. A framework for automated analysis and simulation of 3D polycrystalline microstructures. Part 2: Synthetic structure generation. Acta Mater. 2008;56(6):1274–87.
[91] Wusatowska-Sarnek AM, Ghosh G, Olson GB, Blackburn MJ, Aindow M. Characterization of the microstructure and phase equilibria calculations for the powder metallurgy superalloy IN100. J Mater Res 2003;18(11):2653–63.
[92] Shenoy M, Zhang J, McDowell DL. Estimating fatigue sensitivity to polycrystalline Ni-base superalloy microstructures using a computational approach. Fatigue Fract Eng Mater Struct 2007;30(10):889–904.
[93] Dalaei K, Karlsson B. Influence of shot peening on fatigue durability of normalized steel subjected to variable amplitude loading. Int J Fatigue 2012;38:75–83.
[94] Holzapfel H, Schulze V, Vohringer O, Macherauch E. Residual stress relaxation in an AISI 4140 steel due to quasistatic and cyclic loading at higher temperatures. Mater Sci Eng 1998;A248:9–18.

[95] Wick A, Schulze V, Vohringer O. Effects of warm peening on fatigue life and relaxation behaviour of residual stresses in AISI 4140 steel. Mater Sci Eng 2000;A293:191–7.
[96] Zhuang WZ, Halford GR. Investigation of residual stress relaxation under cyclic load. Int J Fatigue 2001;23(Supplement 1):S31–7.
[97] Zaroog OS, Ali A, Sahari BB, Zahari R. Modeling of residual stress relaxation of fatigue in 2024-T351 aluminium alloy. Int J Fatigue 2011;33(2):279–85.
[98] Gariepy A, Bridier F, Hoseini M, Bocher P, Perron C, Levesque M. Experimental and numerical investigation of material heterogeneity in shot peened aluminum alloy AA2024-T351. Surf Coat Technol 2013;219:15–30.